

LOCALIZATION OF SHORT DURATION GRAVITATIONAL-WAVE TRANSIENTS WITH THE EARLY ADVANCED LIGO AND VIRGO DETECTORS

REED ESSICK¹, SALVATORE VITALE¹, ERIK KATSAVOUNIDIS¹, GABRIELE VEDOVATO², SERGEY KLIMENKO³

Draft version September 16, 2018

ABSTRACT

The Laser Interferometer Gravitational wave Observatory (LIGO) and Virgo, advanced ground-based gravitational-wave detectors, will begin collecting science data in 2015. With first detections expected to follow, it is important to quantify how well generic gravitational-wave transients can be localized on the sky. This is crucial for correctly identifying electromagnetic counterparts as well as understanding gravitational-wave physics and source populations. We present a study of sky localization capabilities for two search and parameter estimation algorithms: *coherent WaveBurst*, a constrained likelihood algorithm operating in close to real-time, and *LALInferenceBurst*, a Markov chain Monte Carlo parameter estimation algorithm developed to recover generic transient signals with latency of a few hours. Furthermore, we focus on the first few years of the advanced detector era, when we expect to only have two (2015) and later three (2016) operational detectors, all below design sensitivity. These detector configurations can produce significantly different sky localizations, which we quantify in detail. We observe a clear improvement in localization of the average detected signal when progressing from two-detector to three-detector networks, as expected. Although localization depends on the waveform morphology, approximately 50% of detected signals would be imaged after observing 100-200 deg² in 2015 and 60-110 deg² in 2016, although knowledge of the waveform can reduce this to as little as 22 deg². This is the first comprehensive study on sky localization capabilities for generic transients of the early network of advanced LIGO and Virgo detectors, including the early LIGO-only two-detector configuration.

Subject headings:

1. INTRODUCTION

Advanced ground-based gravitational-wave detectors, such as the two advanced LIGO observatories [Harry & the LIGO Scientific Collaboration (2010)] and advanced Virgo [Accadia et al. (2012)], will begin collecting data as early as 2015. Although the detectors will not operate at design sensitivity initially, they will operate with enough sensitivity to possibly detect the first gravitational-wave transients [J. Aasi (2013)]. This promises many scientific boons, and accurate waveform reconstruction and parameter estimation will be key in extracting as much information as possible from these detections. In particular, accurate measurements of the sources' positions on the sky can help determine their populations, their distributions, and possible formation mechanisms [Dominik et al. (2012); Kelley et al. (2010); Belczynski et al. (2014)]. Furthermore, accurate sky localization will help electromagnetic follow-up to gravitational-wave transients, which may bring gravitational-wave observations into astrophysical and cosmological context. This has been carefully studied for some binary systems [Singer et al. (2014)], and possible counterparts have been proposed [Metzger & Berger (2012); Barnes & Kasen (2013)].

Searches for gravitational-wave transients are well motivated astrophysically. Among them, gravitational waves generated by compact binary systems are the best understood, with well studied and modeled waveforms. Therefore, searches targeting compact binary systems

employ matched filtering techniques [Abadie (2012a)]. Although significant effort has been invested in analytical and numerical studies of expected waveforms from compact binaries [Ajith et al. (2005, 2011); Damour & Nagar (2008); Hannam et al. (2010); Sturani et al. (2010); J Aasi (2014); Cannon et al. (2013)], some uncertainties still exist, particularly in binary black hole systems with spin or large eccentricity. Several of the anticipated transient sources come with only poorly understood or phenomenological gravitational waveforms, such as gravitational radiation from core-collapse supernovae [Ott (2009)]. These waveforms are typically extremely difficult to simulate, and in the case of supernovae, may be subject to stochastic processes that make templated searches difficult. Other transient gravitational-wave sources include pulsar glitches, starquakes associated with magnetars, and cosmic string cusps [Abadie (2012b)]. In addition, there is always the possibility of completely unanticipated signals from currently unknown sources. Generic transient searches that make only minimal assumptions on the signal's morphology (waveforms, polarizations) are well suited to detect such sources and, in this way, complement matched-filtering approaches [Abadie (2012b)].

In this study, we focus on short-duration (less than one second) gravitational-wave transients, also referred to as bursts, which are typically un-modeled or poorly modeled. Moreover, we focus on source localization only, rather than waveform reconstruction, and attempt to quantify the expected uncertainties produced by analysis of gravitational wave data in the early advanced detector era. In order to assess the performance of our algorithms,

¹ MIT LIGO Laboratory

² INFN Padova

³ University of Florida

we use families of ad hoc waveforms as a proxy for what may accompany astrophysical events [Abadie (2012b)].

We used three ad-hoc signal morphologies and along with Binary Black Hole (BBH) coalescences to explore a wide range of possible signals detectable by generic burst searches. The ad-hoc morphologies scan the signal phase-space with templates possessing both small and large time-frequency areas that span the entire sensitive frequency band of the instruments. Such waveforms should approximate the localization of signals from possible burst sources like core-collapse supernovae. Depending on the mechanism [Ott (2009)], their waveforms may resemble high- Q sine-Gaussian signals (like in the acoustic mechanism [Burrows et al. (2006, 2007); Ott et al. (2006)]), millisecond-scale Gaussian-like peaks (as in simulations of the rotating collapse and bounce in CCSNe [Dimmelmeier et al. (2008)] or even white-noise bursts (if turbulent convection takes place [Ott (2009)]). Recent studies have focused on inferring the explosion mechanism from gravitational waveforms [Logue et al. (2012)], although they did not address localization. Furthermore, using a range of morphologies allows us to characterize localization for generic signals which may come from unanticipated sources. This work is analogous to a recent study focusing on binary neutron star (BNS) coalescences [Singer et al. (2014)]. Signals from such systems typically have longer signal durations with well known broadband waveforms and are targeted more optimally with matched filter searches [Abadie (2012a)].

Accurately localizing gravitational wave signals can shed light on the sources' distribution across the sky and possibly lead to identification of counterparts throughout the electromagnetic spectrum. Again, this has been carefully considered for a few scenarios [Feng et al. (2014); Evans (2012); Aasi (2014a)] but is difficult to address for un-modeled bursts. However, accurate characterization of gravitational wave localization will naturally inform any electromagnetic follow-up effort. [There exist a host of possible counterparts to generic gravitational wave bursts. For instance, core-collapse supernovae in the local universe are expected to produce detectable gravitational radiation [Ott (2009)] and will have bright counterparts throughout the electromagnetic spectrum as well as in low-energy neutrinos [Scholberg (2012)]. Superconducting cosmic string cusps are expected to produce both gravitational [Aasi (2014b)] and electromagnetic radiation [Vachaspati (2008)]. BBH systems may or may not produce electromagnetic counterparts, depending on the system's environment. For BBH systems in a clean environment, gravitational-wave data may be the only way to study these systems. Furthermore, coincident electromagnetic observations for bursts from unknown sources will be invaluable in determining the associated physical system. Regardless of the source of gravitational radiation, electromagnetic and neutrino observations may place the event in an astrophysical context.

Although several algorithms provide source localization estimates, we focus on Coherent WaveBurst (cWB) [Klimentko et al. (2005, 2008)], a constrained likelihood algorithm (Section 3.1), and LALInferenceBurst (LIB) [Aasi et al. (2013); Veitch et al. (2014); LIGO Scientific Collaboration, Virgo Collaboration (2014)], a Markov chain Monte Carlo (MCMC) parameter estimation algorithm (Section 3.2). Previous sky localization

studies for un-modeled bursts used an earlier version of cWB and investigated networks with three or more detectors [Klimentko et al. (2011); J. Aasi (2013); Markowitz et al. (2008); LIGO Scientific Collaboration et al. (2012)]. Furthermore, these studies typically focused on a few sample waveforms with a few fixed parameter values. This includes characterizing algorithmic performance as a function of injection amplitude, for example. We focus on ensemble averages computed over a population of events with randomly selected parameters and with the expected detector configurations for the first two years of the advanced detector era. In particular, we generate an astrophysical population of generic burst events that extends beyond the detectors' sensitivity limits. This characterizes the localization capabilities for typical events, and models the relative frequency of "loud" signals versus the more common "quiet" signals. This population yields estimates that describe a "typical expected event" from gravitational-wave detectors. We present an analysis of sky localization during the transition from two detectors (LIGO-Hanford and LIGO-Livingston in 2015) to three detectors (LIGO-Hanford, LIGO-Livingston and Virgo in 2016) with expected noise curves made available by the LIGO and Virgo collaborations [J. Aasi (2013)].

Unlike many electromagnetic observations, gravitational-wave source position uncertainties are very large, typically larger than 100 deg^2 . Therefore, gravitational-wave searches produce probability distributions over the sky, rather than single locations, from which meaningful quantities are derived. These probability distributions can have very complicated shapes, including severe fragmentation and spatially separated support. A thorough understanding of these distributions can inform the design of follow-up programs as well as the choice of which events should be pursued.

This paper is organized as follows: Section 2 describes the simulated noise and gravitational waveforms we use in this study; Section 3 briefly describes the two algorithms we use; Section 4 discusses the observed localization capabilities of the two pipelines over the same set of detected signals; Section 5 describes some systematics associated with these algorithms and we conclude in Section 6.

2. DATA PREPARATION

2.1. Noise

We use simulated stationary Gaussian noise throughout this study. Expected noise curves for the two LIGO detectors and Virgo are shown in Figure 1, which plots the curves for LIGO in 2015, 2016 and at design sensitivity as well as Virgo curves in 2016 and at design sensitivity. The 2015 and 2016 curves were chosen as the geometric mean of the optimistic and pessimistic estimates in [J. Aasi (2013)], and the actual improvement in the noise curves will depend on the commissioning of the detectors. While these curves may not be realized exactly, they provide a good estimate for the Gaussian noise expected in the advanced detector era.

Another important source of noise, particularly for burst searches, is *non-Gaussian* in nature. These non-Gaussian artifacts ("glitches") form a long tail at high amplitudes, reducing the sensitivity of searches [J. Smith

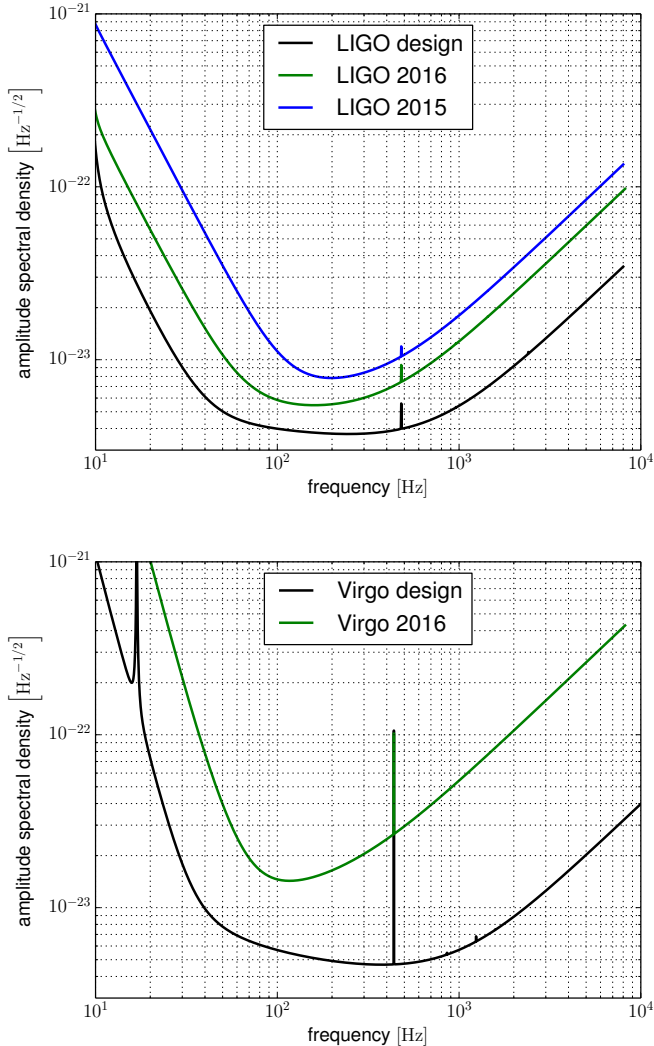


FIG. 1.— Expected amplitude strain noise for advanced detectors in 2015, 2016 and at design sensitivity. The resonances correspond to suspension “violin” modes near 500 Hz and “bounce” modes near 15 Hz. The bounce mode is within the seismic wall for the LIGO curves.

(2014)]. Because we simulate only Gaussian noise, we do not have glitches present in our data. However, the presence or absence of glitches will not affect our study. For a given event, glitches affect a gravitational-wave observer’s confidence that this particular event is of astrophysical origin, but will not affect the pipeline’s ability to localize true astrophysical events.

Furthermore, we do not simulate realistic detector live-times because we do not attempt to make a statement about detection rates. Instead, we use one month of continuous simulated noise for each of the 2015 and 2016 runs.

2.2. Injections

Several signal morphologies were used in an attempt to simulate a wide range of possible gravitational-wave transients. While these are not meant to be examples of actual astrophysical signals (with the exception of compact binary systems), historically several exemplary waveforms have been used to approximate generic

burst events [J. Aasi (2013); Klimentko et al. (2011); Markowitz et al. (2008)]. We focus on generic waveform morphologies because they allow us to test our ability to localize very different signals without specializing to a specific source. In this study we use four signal morphologies: Sine-Gaussian (SG), Gaussian (G), White-Noise Bursts (WNB), and Binary Black Hole approximants (BBH) with spins (anti-)aligned with the orbital angular momentum. The parameter ranges were chosen as reasonable given the typical frequencies probed by burst searches (32 – 2048 Hz) as well as the expected noise curves. The parameters were drawn independently, and Table 4 lists the exact values used.

In particular, we distribute our injections as if they were astrophysical, i.e., uniform in comoving volume. In addition, the quietest signals were chosen to be just below the detector’s maximum sensitivity. This ensures that the signals recovered were limited by the detector’s sensitivity rather than an artificial threshold. All populations were distributed uniformly over the sky and regularly spaced in time.

As mentioned above, we distribute our injections uniformly in comoving volume. This is done using standard Λ CDM cosmology ($\Omega_m = 0.3$, $\Omega_\Lambda = 0.7$). If we take supernova as typical energy scales for un-modeled bursts, an optimistic upper limit for the energy emitted as gravitational waves is $E_{GW} \sim 10^{-4} M_\odot c^2$ [Ott et al. (2006)]. If we assume a energy scale ten times larger is associated with and isotropically radiated SG with $f_o = 200$ Hz, this yields a horizon distance of ~ 3.8 Mpc with advanced LIGO design sensitivity. At this distance, the difference between volume and comoving-volume is negligible ($\sim 0.1\%$). Therefore, we distribute SG, G, and WNB signals uniformly in volume.

Furthermore, because we do not have an exact energy scale for generic (un-modeled) transient events, it is difficult to compute a distance. We expect the signal amplitude to scale inversely with the luminosity distance, and this can be used to define a distribution over $h_{rss}^2 = \int dt (h_+^2 + h_\times^2)$ given a distribution over distance. A derivation is provided in the Appendix, but we can model a uniform-in-volume distribution as

$$p(D_L) \propto D_L^{-2} \Rightarrow p(h_{rss}) \propto h_{rss}^{-4} \quad (1)$$

BBH systems should be detectable at several Gpc, and the difference between volume and comoving volume is non-trivial here ($\geq 70\%$). For the BBH signals, we have a well defined distance and distribute the signals uniformly in comoving volume.

2.2.1. Sine-Gaussian waveforms

Sine-Gaussian (SG) waveforms have historically been used by the LIGO and Virgo Collaborations to simulate generic bursts [Abadie (2012b)]. We define our SG waveforms according to Equations 2 and 3 . f_o is the central frequency of the Sine-Gaussian; τ is the width in the time domain. α controls the relative weights between the two polarizations. This is equivalent to choosing the coordinate system in the wave-frame relative to the Earth-fixed detector frame.

$$h_{\times}(t) = \sin(\alpha) \frac{h_{r_{ss}}}{\sqrt{Q(1-\cos(2\phi_o)e^{-Q^2})/4f_o\sqrt{\pi}}} \sin(2\pi f_o(t-t_o) + \phi_o) e^{-(t-t_o)^2/\tau^2} \quad (2)$$

$$h_{+}(t) = \cos(\alpha) \frac{h_{r_{ss}}}{\sqrt{Q(1+\cos(2\phi_o)e^{-Q^2})/4f_o\sqrt{\pi}}} \cos(2\pi f_o(t-t_o) + \phi_o) e^{-(t-t_o)^2/\tau^2} \quad (3)$$

2.2.2. Gaussian waveforms

We also inject Gaussian envelopes in the time domain (G), defined by Equations 4 and 5. These can be considered as limiting cases of SG waveforms in which $f_o \rightarrow 0$. However, removing the oscillatory component means the frequency domain waveform is a Gaussian centered about $f = 0$, and the signal is detected essentially by the Gaussian's wings. Because the seismic wall in the noise spectra at low frequencies is very steep, small changes in Gaussian width can significantly affect detectability. This and the lower bound on signal duration from the pipeline's sampling rate determined the injection popu-

lation's parameter ranges.

$$h_{\times}(t) = \sin(\alpha) \frac{h_{r_{ss}}}{\sqrt{\tau}} \left(\frac{2}{\pi}\right)^{1/4} e^{-(t-t_o)^2/\tau^2} \quad (4)$$

$$h_{+}(t) = \cos(\alpha) \frac{h_{r_{ss}}}{\sqrt{\tau}} \left(\frac{2}{\pi}\right)^{1/4} e^{-(t-t_o)^2/\tau^2} \quad (5)$$

2.2.3. White-Noise Burst waveforms

Perhaps one of the most generic waveforms we investigate is the white-noise burst (WNB), defined by Equations 6 and 7.

$$h_{\times}(t) \propto e^{-(t-t_o)^2/\tau^2} \int e^{-2\pi ift} [\Theta(f - f_{min}) - \Theta(f - f_{max})] df \quad (6)$$

$$h_{+}(t) \propto e^{-(t-t_o)^2/\tau^2} \int e^{-2\pi ift} [\Theta(f - f_{min}) - \Theta(f - f_{max})] df \quad (7)$$

The flat frequency domain component is randomly drawn from Gaussian white noise rather than a truly flat curve. All parameters besides $h_{r_{ss}}$ are drawn first, including this randomly sampled frequency domain waveform, and then the amplitude is scaled appropriately to obtain the desired $h_{r_{ss}}$. These signals are meant to simulate an excess of power randomly distributed within some frequency band and localized in time.

2.2.4. Binary Black Hole waveforms

We simulate the inspiral of massive binary systems because they coalesce at relatively low frequencies. This means that the signal is relatively compact in the frequency domain, and generic burst searches can more easily detect these signals compared to lighter systems. We expect burst searches to have sensitivity to Binary Black Hole (BBH) coalescence at cosmological distances.

We use Inspiral-Merger-Ringdown (IMR) phenomenological approximants to model BBH coalescence [Ajith et al. (2011); Hannam et al. (2010)]. These waveforms are constructed by stitching analytic post-Newtonian expansions, accurate to 3.5 PN orders, with numerical-relativity results for merger and analytic quasi-normal modes for ringdown. Typically, the inspiral portion of the waveform is known much more accurately than the merger and ringdown. However, our BBH signals contain massive components and their mergers occur within the detector's sensitive band.

Importantly, our simulated waveforms also incorporate the affects of spin-orbit coupling. We focus on spins (anti)-aligned with the orbital angular momentum, so there is no spin-precession in these waveforms. There is still uncertainty about the efficiency of common envelop evolution and the relative importance of supernova kicks

[Belczynski et al. (2014)], and astrophysical BBH systems may or may not have their spins (anti)-aligned with the orbital angular momentum. However, this is a reasonable assumption when characterizing our algorithms' performance.

We use a range of component masses consistent with stellar mass black holes. We also simulate a wide range of spin magnitudes for each object.

3. LOCALIZATION PIPELINES

The goal of sky localization of gravitational-wave transients is to construct a posterior probability distribution over the sky. We use two pipelines to localize signals: Coherent WaveBurst (cWB) and LALInferenceBurst (LIB). Each pipeline attempts to reconstruct the signal's sky position in a different way, which we briefly describe.

3.1. Coherent WaveBurst

Coherent WaveBurst (cWB) is a data analysis algorithm for the detection of transient gravitational-wave signals (bursts) [Klimenko et al. (2005, 2008)]. In cWB, burst events are identified as excess power patterns, exceeding some threshold, in the time-frequency domain obtained via a wavelet transformation. Assuming Gaussian noise, cWB combines data from multiple detectors to compute a constrained likelihood functional dependent on the sources sky position. For networks with two or three detectors, strong degeneracies exist in the likelihood and cWB applies several ad-hoc constraints to limit the signal space. The constrained likelihood is maximized over all possible gravitational-wave signals for each point in the sky, and several statistics are computed at each point. cWB generates maps by combining these

statistics, which are used to approximate posterior probability distribution over the sky [Klimentko et al. (2011)]. Previous studies [J. Aasi (2013); Klimentko et al. (2011)] used an earlier version of cWB. We present results from an updated version of the algorithm, referred to as the second-generation: cWB-2G [Klimentko (2014)].

Importantly, this study implements an *effective prior* on the source position in Earth-fixed coordinates. This is the first implementation of such prior for burst detection algorithms, which modulate the posterior with the detectors antenna patterns to incorporate the fact that quieter signals are more frequent than loud signals. It is, therefore, more likely a priori to detect signals from parts of the sky with large antenna patterns. A derivation is provided in the Appendix.

cWB uses two network constraints (regulators), which incorporate prior knowledge on how the network responds to generic gravitational-wave signals. The network response to a signal is constrained by the antenna patterns; this is used in cWB’s analysis to “regulate” reconstructed signal waveforms and reduce the algorithms sensitivity to non-Gaussian noise artifacts. The regulators modify the form of the likelihood functional and can be thought of as non-trivial priors. In cWB-2G, the regulators are controlled by the parameters δ and γ . δ controls the permissible ratios between the contributions to the likelihood from separate polarizations, and γ acts as the lower bound on the correlation between the detectors [Klimentko (2014)]. While the regulators are not needed to reject background in our simulated Gaussian noise, they will be used in an actual observing run. Section 7.2 describes the exact parameters used.

With two detectors, our choice of regulator settings force cWB to reconstruct only a single polarization. Because the Hanford and Livingston detectors are nearly aligned, they are effectively sensitive to only a single polarization [Klimentko et al. (2011); Sutton et al. (2010)] and this is a reasonable approximation. The three-detector regulators are almost, but not quite, turned off. We discuss the features introduced by the regulators in Section 5.

While false-alarm rates will depend on the Gaussian and non-Gaussian noise in an observing run, we chose detection thresholds for cWB that correspond to a false alarm rate of 1 per year in historical non-Gaussian noise. This threshold may not be high enough to claim a confident detection, but it is likely that events satisfying such criterion will be of significant interest.

cWB is a low-latency pipeline, typically run as an online search. Posteriors are produced as part of the detection pipeline, and are available within minutes of recording the data.

3.2. *LALInferenceBurst*

LALInferenceBurst (LIB) is a Bayesian Markov chain Monte Carlo parameter estimation algorithm designed to recover burst signals and estimate some key signal parameters, including sky position. LIB is based on nested sampling and shares most of its libraries with LALInference, its counterpart for parameter estimation of compact binary coalesces (CBC) [Veitch et al. (2014)]. A detailed description of nested sampling and its application to gravitational-wave parameter estimation can be found elsewhere [Skilling (2004); Veitch & Vecchio (2010)].

The main difference between the CBC and Burst version of LALInference is that, while the CBC version filters the data using long waveforms that describe the signal emitted by compact binaries, LIB uses a single SG waveform.⁴ This implies that LIB can not perfectly match some of the simulated signals considered in this study, such as WNB and BBH. We expect LIB to perform sub-optimally for these signals, while it should still be able to recognize that a coherent signal is present, and produce useful sky localization information. We see that this is indeed the case.

LIB has a larger computational cost than cWB, and it typically cannot be run as a blind search algorithm. Instead, LIB is run as a follow-up to pre-selected times, with typical latencies between hours and days. It provides flexibility in tuning computational cost and sensitivity. With the configuration used in this analysis, 50% of the events were processed within two hours. However, a detection decision can be reached with latencies of a few minutes. For this study, LIB was run on a subset of triggers detected by cWB and was not used as a search pipeline [Vitale (2014)]. Beside the approximate time of an event, LIB does not use any data products produced by cWB.

Because LIB is a template based algorithm, we can put priors on the (relatively few) parameters that describe the template. In this work, we put a uniform-in-volume prior on the template amplitude, $p(h_{rss}) \propto h_{rss}^{-4}$. This is a more direct way of incorporating the prior knowledge than the effective prior used with cWB, but the information content is similar. The prior furthermore assumes that sources are uniformly distributed on the sky, and modulation with the antenna patterns is achieved only through the prior on signal amplitude. The prior on other signal parameters was flat with ranges larger than the injected ranges. Section 7.2 describes the exact parameters used.

4. RESULTS

While localizing sources using gravitational-wave data alone is important, past studies have emphasized direct electromagnetic follow-up [LIGO Scientific Collaboration et al. (2012); Abadie (2012c)]. Therefore, the metrics used to evaluate localization at least tacitly assume some electromagnetic follow-up program. We present results for a few standard measures for our simulations of the early advanced detector era.

Before we investigate the posterior distributions produced by cWB and LIB, we should understand typical features of gravitational-wave localization. The majority of sky localization comes from time-of-flight measurements between distantly located detectors. A single detector is sensitive to nearly the entire sky, so it cannot localize sources well. However, because gravitational waves travel at the speed of light, the difference in the times of arrival at spatially separated detectors allow us to triangulate the source location on the sky. Figure 2 sketches a skymap generated with two detectors, in which the locus of source positions consistent with the observed time-of-flight between detectors is a ring. For three detectors,

⁴ It is possible to also use Gaussians or other short waveforms, but we do not consider them in this study.

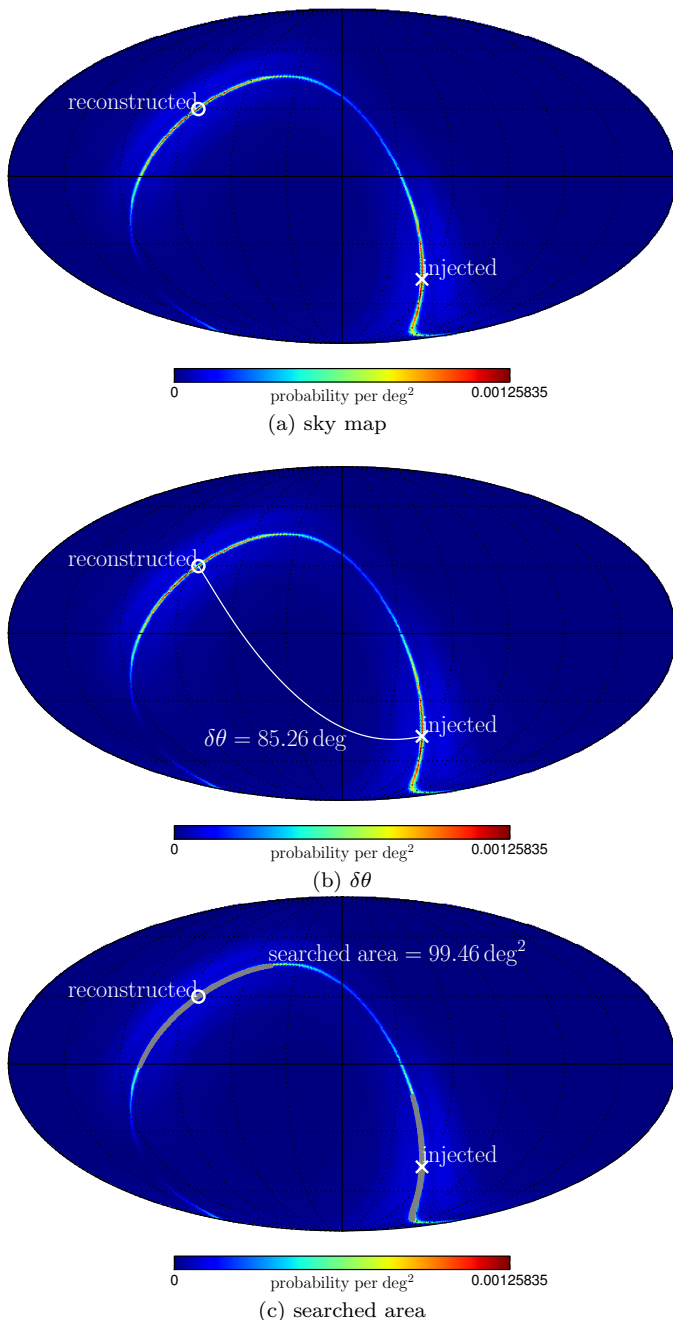


FIG. 2.— Mollweide projections demonstrating the two basic statistics used to quantify sky localization: angular offsets and searched area. (a) The entire posterior with the injected and reconstructed locations marked. In this example, the difference between time-of-arrival in the two LIGO detectors (Livingston, LA and Hanford, WA) was 3 ms. (b) The *angular offset* is defined as the smallest angle swept between the injected location and the reconstructed location (maximum a posteriori), shown here as a geodesic. (c) The *searched area* is defined as the area assigned a probability greater than or equal to the probability assigned to the injected location. In the figure this is the shaded area.

the locus is reduced to two points, and so on.⁵ This triangulation can be thought of as producing a likelihood in the Bayesian sense. Modulation around the ring is achieved through knowledge of the antenna patterns and

⁵ Section 7.4 shows a few sample posteriors produced by each algorithm with our data set.

TABLE 1
SAMPLE SIZES OF DETECTED EVENTS BY MORPHOLOGY AND YEAR.

year	algorithm	morphology			
		G	SG	WNB	BBH
2015	cWB	256	1112	769	2488
	LIB	256	1112	769	500
2016	cWB	417	677	853	6394
	LIB	416	664	851	498

an assumption about the distribution of signal amplitudes. The detector network is simply more sensitive in some directions than others, which means it can detect more signals from certain directions. This is included in the effective prior for cWB and the prior on template amplitude for LIB. Figure 2(a) demonstrates this with clear hot spots on the ring, although the entire ring is visible.

Table 1 shows the number of detected events. We injected roughly 100,000 events for each morphology in each detector network. The low number of recovered signals reflects the uniform-in-volume distribution of the signals, which causes the majority of signals to be very distant and too quiet to be detectable. Both cWB and LIB were run over the same events. We use all events detected by cWB for G, SG, and WNB morphologies in both years. However, due to the large sample of detected BBH injections, we randomly select 500 events to process with LIB. This gives us an accurate representation of LIB's performance with slightly larger errors.

4.1. Angular offset

Perhaps the simplest measure of localization is the angle between the *maximum a posteriori* and the source's position ($\delta\theta$). Figure 2(b) shows this for a cartoon posterior, and the line represents a geodesic connecting the injected and reconstructed locations. In this example, the angle is large because the reconstructed location is placed on the wrong side of the ring.

Figure 3 shows the observed distributions of this statistic. We use $\cos(\delta\theta)$ to highlight grouping around $\delta\theta = 0^\circ, 180^\circ$ corresponding to the true and antipodal positions of the source, respectively. There is improvement when transitioning from the two-detector network to the three-detector network, although it is not drastic. This is because Virgo is less sensitive than the two LIGO detectors, and many detected events are essentially detected by only two detectors.

In the 2015 network, both algorithms place signals close to $\cos(\delta\theta) = \pm 1$ and produce a desert in between. This symmetry is due to the nearly aligned antenna patterns for the two LIGO detectors, which makes the antipode degenerate with the correct side of the sky. This symmetry is a generic feature of the detector's antenna patterns and also appears when the morphology is known a priori [Singer et al. (2014)]. In the 2016 network, there is some reduction in the mode near $\cos(\delta\theta) = -1$. We note that the peak near $\delta\theta \sim 0$ is sharper in 2016 than in 2015, however the median value of $\delta\theta$ is actually larger in 2016 for cWB ($\sim 33^\circ$ compared to 23° for WNB). This may be due to the regulators (see Section 5). In the three-detector network, there is a degeneracy in the posteriors associated with reflections about the plane de-

fined by the three detectors [J. Aasi (2013); Fairhurst (2009)]. This degeneracy may be responsible for some of the antipodal population as well. This can be seen in the LIB distributions, which show the degeneracy but also show a decrease in the median $\delta\theta$ in the 2016 network, as expected.

We also note that the general features of source localization by both cWB and LIB do not depend strongly on the signal morphologies. This is significant, as it suggests that the same localization algorithm can be used to construct posteriors for generic bursts without waveform-specific biases.

Typically, we expect $\cos(\delta\theta) \rightarrow 1$ in the limit of high SNR. This holds for the three-detector network, in which the signal is triangulated to the true location, and degeneracy from reflections by the plane of the detectors are broken by the antenna patterns. However, this is not the case in the two-detector network. This is because, even in the limit of high SNR, the two-detector network cannot break the ring-degeneracy in the posterior. If the waveform is not known a priori, then it must be reconstructed. For the two-detector network, different points along the triangulation ring correspond to different reconstructed waveforms. However, they all reproduce the data equally well and the algorithm does not prefer one location on the ring over another. In fact, only the width of the ring decreases as SNR increases.

Tables 2 and 3 give cumulative fractions of events with $\delta\theta$ less than a few exemplar values.

4.2. Searched area

Another measure of source localization is the *searched area*. We define this as the area on the sky assigned a probability greater than or equal to the probability assigned to the injected location [LIGO Scientific Collaboration et al. (2012)]. If a follow-up algorithm sorts through an list of pixels ordered by probability, this approximates the amount of area imaged before finding the injection. Importantly, the searched area does not account for spatially separated support in the posterior distribution. Figure 2(c) demonstrates this statistic as the shaded area. We can estimate the fraction of events for which electromagnetic counterparts will be observed within a given area with a cumulative distribution over the searched area.⁶

Figure 4 shows cumulative distributions of observed searched areas for all morphologies considered. Importantly, we see that the searched area improves when moving from the two-detector network in 2015 to the three-detector network in 2016, even though the Virgo noise curve is nearly twice as high as the LIGO curves in 2016. This can be attributed to a more informative likelihood, and is true for both algorithms.

We also see that LIB performs much worse than cWB for WNB signals. This is due to template mis-match within LIB, which attempts to model all signals with a single SG template. In fact, LIB assigns a few WNB signals searched areas equal to the entire sky. This is

⁶ Another possible observing plan would be to set a confidence regions, say 50%, rather than a fixed area. We could then determine the fraction of events with 50% confidence regions containing less than a given area. We avoid this statement here because the posteriors produced by cWB and sometimes LIB are poorly calibrated (see section 5).

because the random WNB waveform matches so poorly with the SG template that LIB does not detect the signal.

In 2015, both algorithms perform nearly identically for both SG and G waveforms. This reflects the fact that we cannot construct posteriors for burst signals more accurately than a timing ring modulated by the antenna patterns. LIB outperforms cWB for the smallest searched areas and for SG signals, as expected given the waveform basis used in LIB. However, the fact that both algorithms agree over a wide range of searched areas suggests there is only minimal improvement possible with knowledge of the actual signal morphology.

In 2016, LIB localizes G and SG signals better than cWB. This is because LIB uses SG templates to recover signals, while cWB does not. Therefore, knowledge of the correct signal morphology can significantly improve localization in three-detector networks. However the performance between the algorithms is more comparable for BBH signals.

We also note that WNB are localized consistently better than SG, G, or BBH with cWB. This should not be surprising. A simple Fisher matrix computation like those in [Fairhurst (2009, 2011)] shows that, for SG signals, the expected errors in time-of-flight between detectors should scale as

$$\sigma_t^2 \sim \frac{1}{\rho^2} (f_o^2 + \tau^{-2})^{-1}. \quad (8)$$

τ^{-1} is related to the signal's bandwidth, and therefore we expect high frequency, high bandwidth signals to have the smallest timing errors. From our injections, WNB signals will typically have higher frequencies than G and larger bandwidths than SG. This means they will have smaller timing errors and narrower triangulation rings.

Tables 2 and 3 give cumulative fractions of events with searched area less than a few exemplar values. Unlike $\cos(\delta\theta)$, we see a strong decrease in the searched area in the limit of high SNR in both 2015 and 2016. This is expected from simple triangulation, and corresponds to a narrowing of the triangulation ring in the two-detector case rather than the removal of the ring.

4.3. Extent of the posterior's support

While the searched area and $\delta\theta$ are good indicators of the localization, they do not describe the entire posterior. For example, both the searched area and $\delta\theta$ may be small, suggesting a compact posterior distribution. However, the little area that is included may be scattered across the sky, with a small $\delta\theta$ merely fortuitous. This could correspond to a very narrow ring in the two-detector case, with the reconstructed location placed next to the injected location by chance.

To diagnose the prevalence of such cases, we plot the maximum angular distances from the injection's source to any point in the searched area ($\delta\theta_{inj}$) in Figure 5. If an electromagnetic follow-up is carried out systematically over this area, this estimates the separation between points in the region searched before imaging the source. In particular, we should be able to determine whether the posterior has support at antipodal points in the sky, which are difficult to observe with a single telescope.

Figure 5 shows that there is support near the antipode for a large fraction of events in 2015. This indicates that

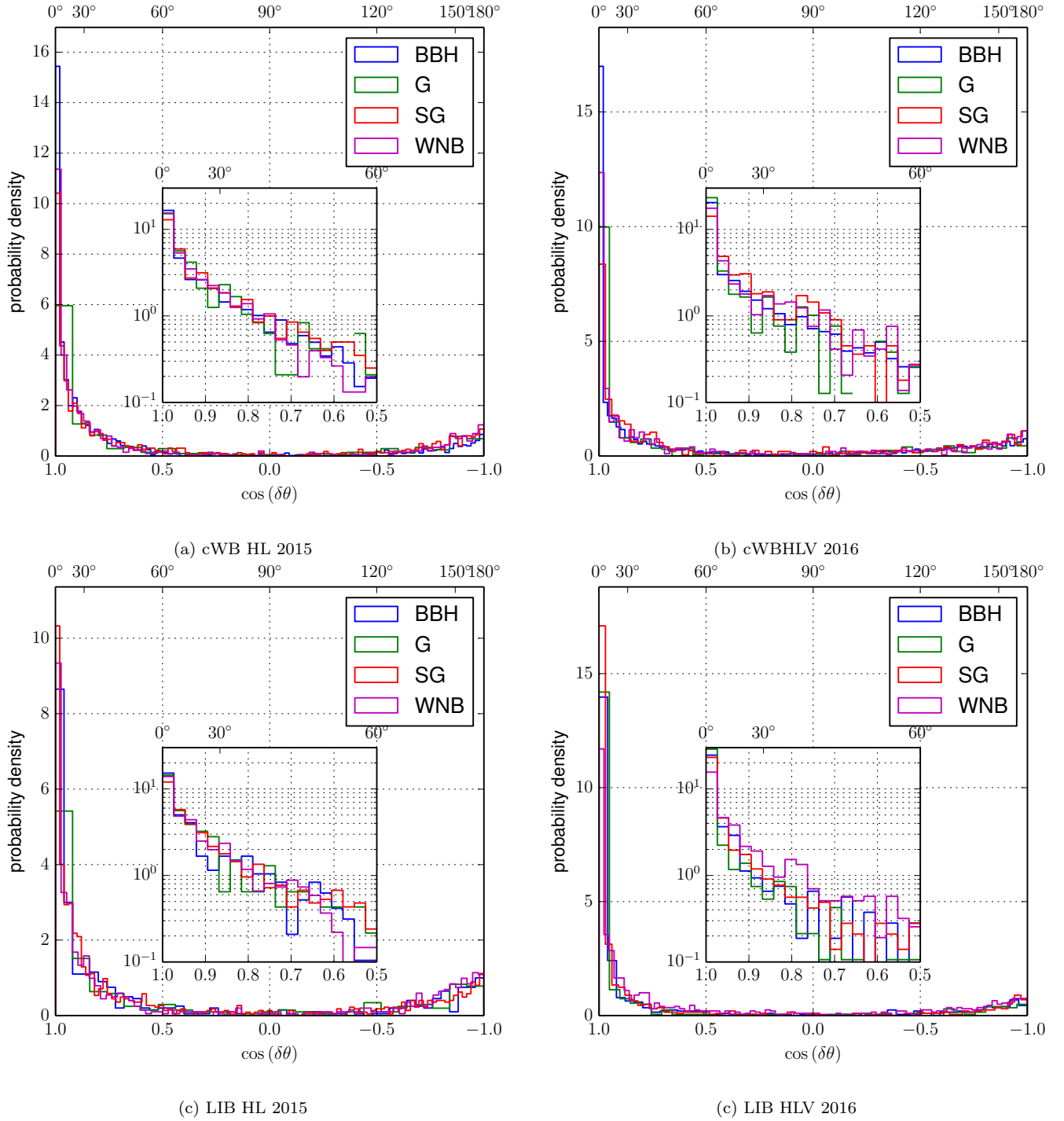
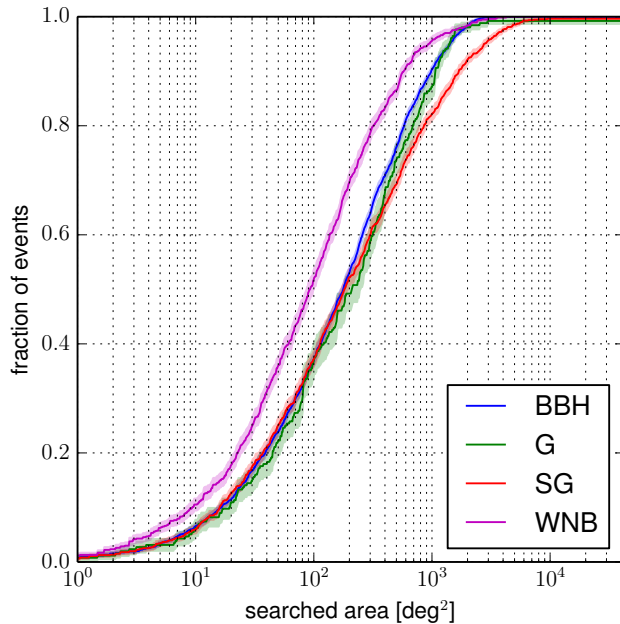
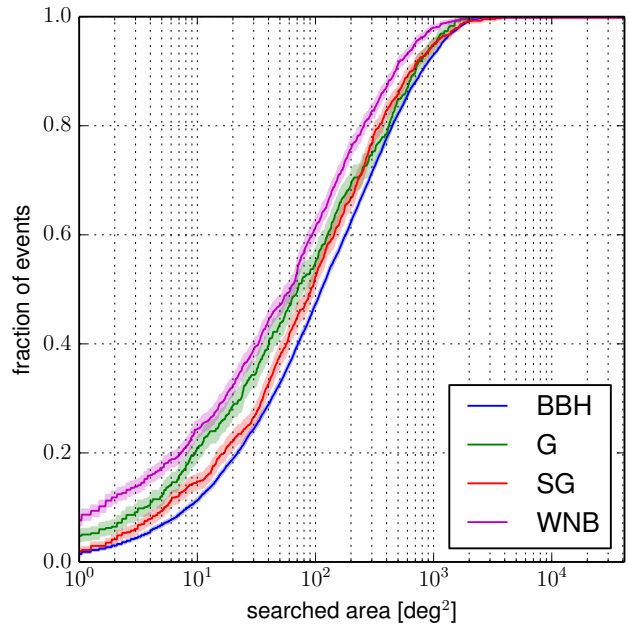


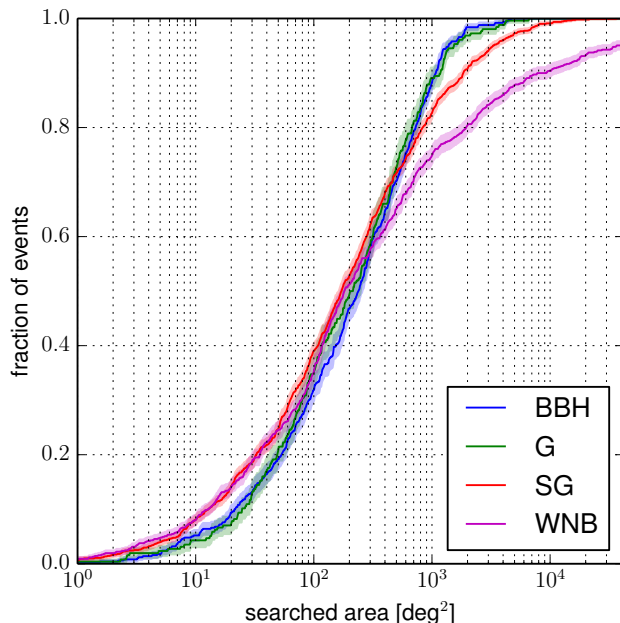
FIG. 3.— Normalized histograms of $\cos(\delta\theta)$, where $\delta\theta$ is the angle between the injected location and the maximum of the posterior. (a,c) 2015 detector network. (b,d) 2016 detector network. (a,b) cWB. (c,d) LIB.



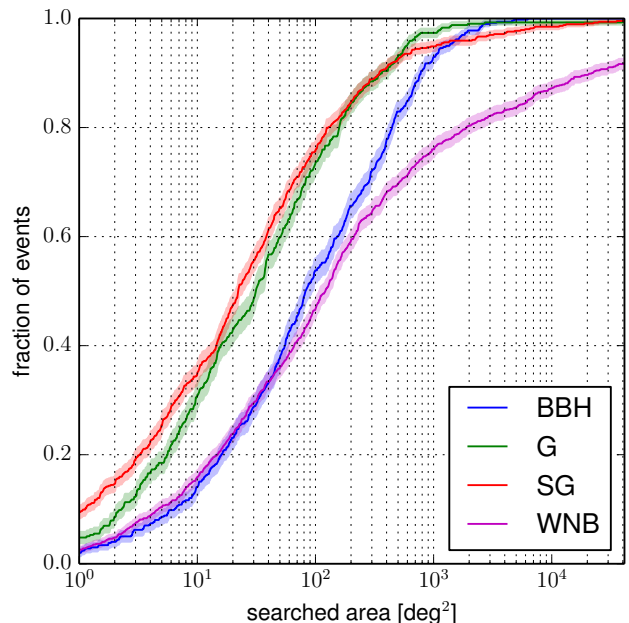
(a) cWB HL 2015



(b) cWB HLV 2016



(c) LIB HL 2015



(d) LIB HLV 2016

FIG. 4.— Cumulative histograms of searched areas for (a,c) 2015 HL and (b,d) 2016 HLV; (a,b) cWB and (c,d) LIB. Shaded regions correspond to 68% confidence intervals.

we will find support all along the degenerate ring modulated by the antenna patterns, which happens to be on the other side of the sky a significant fraction of the time. The lobe near $\delta\theta_{inj} \sim 0^\circ$ corresponds to small searched areas, in which the injection was found quickly before the searched area included points from the antipodal antenna pattern maximum.

The three-detector network shows similar structure. We again see a population of events with small searched areas, with $\delta\theta_{inj} \sim 0^\circ$. Somewhat surprisingly, we see a

large lobe near $\delta\theta_{inj} \sim 180^\circ$. This is likely due to a combination of Virgo's higher noise curve and the reflection degeneracy visible in the $\delta\theta$ distribution as well (Section 4.1). With fewer than four detectors, these antipodal degeneracies may be unavoidable for un-modeled signals.

4.4. Fragmentation

Furthermore, the largest angle between points in the searched area does not tell us about the posterior's shape. Support could be placed along a large ring or randomly

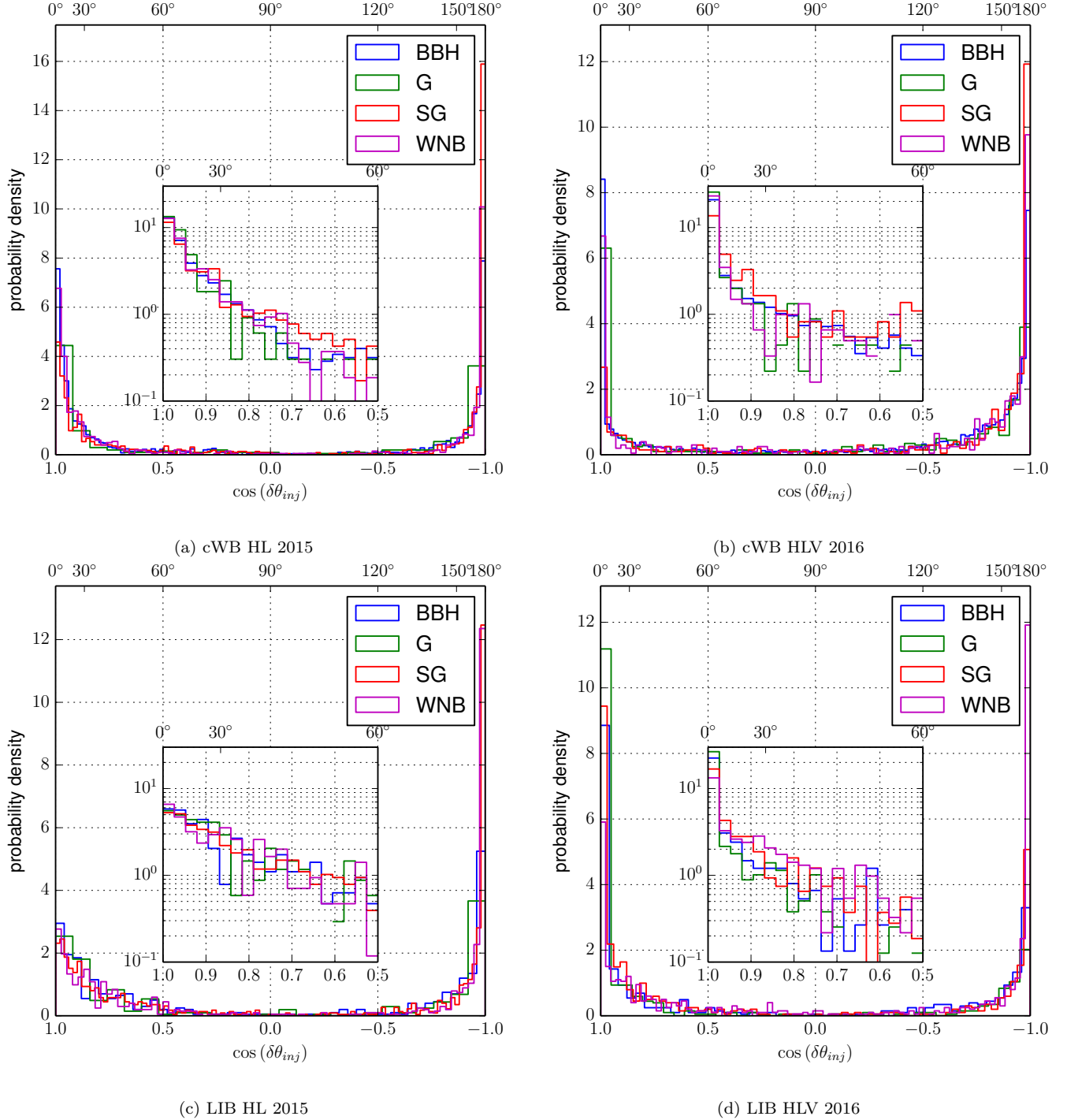


FIG. 5.— Normalized histograms of the largest angle between the source’s true location and any point within the searched area. (a,c) 2015 network. (b,d) 2016 network. (a,b) cWB. (c,d) LIB.

scattered in distant parts of the sky. We call this the fragmentation of the posterior and attempt to measure it by counting the number of disjoint regions within a specified area. For example, if the posterior is split between a blob and it’s antipode, there are two. This is the case for the searched area in Figure 2(c).

Figure 6 shows histograms of the number of simply connected regions within the searched area. There is a lot of morphology dependence, but a few trends are clear. G and BBH signals typically have fewer simply connected

regions than SG and WNB signals. For SG signals, this is because of their strong central frequency and relatively narrow bandwidth.

The oscillatory waveforms imprinted in the data from each detector still match relatively well if they are offset by a small number of cycles, which corresponds to a time-of-flight error between detectors. This causes periodic features in the posterior with typical angular scales of

$\Delta\theta \propto 1/f_o$.⁷ We therefore expect to see parallel rings in two-detector posteriors, and a nearly regular lattice in the three-detector posteriors.

We also note that the WNB signals appear to have fragmentation somewhere between G and SG signals. This is because the WNB signals have wide ranges for their bandwidths relative to their central frequencies. When the bandwidth is comparable to the central frequency, there are no fringe peaks (like a G signal) and when it is narrow compared to the central frequency there are fringe peaks (like a SG signal). BBH signals act similar to G signals because they have relatively broad bandwidths and are concentrated at low frequencies.

4.5. Direct comparison of posteriors

While all the previous statistics allow us to investigate the relative performance of cWB and LIB through ensemble averages, they do not tell us how the sky maps produced by these two methods compare on an event-by-event basis. Comparing localization directly for each event will be important if all algorithms are used to provide alerts and posteriors to the astronomical community.

We first investigate the angular separations between the maxima a posteriori (MAP). There is remarkable agreement in the 2015 data, with the median $\delta\theta_{MAP}$ consistently around 8° . In the 2016 data set there is significantly more disagreement, with the median $\delta\theta_{MAP}$ as high as 84° for some morphologies.

In addition to the angular separation of the maxima a posteriori, we examined the intersection and union of sets of pixels selected by each algorithm. We compute the ratio of intersection to union (i/u) for pixels selected by the two algorithms. Specifically, we compute i/u using 50% and 90% frequentist confidence regions. If i/u is near unity, the maps are very similar and if i/u is close to zero the maps either select nearly disjoint regions or one map includes much more area than the other. In 2015, the median i/u is near 0.5 for both confidence levels. However, there is significantly less overlap in the three-detector network, with i/u between 0.2 and 0.3 even for the 90% confidence region.

We also compute the total size of the spatial support in each posterior for each algorithm. In both the two-detector and three-detector networks, LIB typically assigns non-zero probabilities to many more pixels than cWB. We note that cWB typically assigns a lower confidence to the same region surrounding the maximum a posteriori than LIB. Combining this with the knowledge that cWB typically includes smaller spatial support in its posterior, we come to the conclusion that LIB posteriors typically are strongly peaked with long tails and broad spatial support. cWB posteriors are less peaked, with more uniform probabilities and smaller spatial support.

Additional studies are underway to understand the statistics and systematics of sky maps provided by these methods, not only on injected signals, but also on Gaussian and non-Gaussian noise artefacts.

⁷ The features are not exactly periodic because the signal may vary significantly over time scales comparable to $1/f_o$ and the antenna patterns may favor only part of the sky.

4.6. Summation

Tables 2 and 3 present a synopsis of the searched areas and angular offsets for each morphology and detector configuration. A few example posteriors are plotted in Section 7.4.

We should note that, because the sources of unmodeled burst signals may be unknown, they may not be distributed uniformly in volume. If one takes an agnostic view, they may use only the maximum likelihood estimate without our effective prior. For our injection set, this corresponds to an increase in the median searched areas because the algorithm no longer searches the ring according to the antenna patterns. We tested this using cWB and see that the median searched areas are at least 25% larger (2015 G) without the effective prior, and as much as 59% larger (2015 SG).

Furthermore, we expect BBH signals to be circularly polarized. Incorporating this information into the search should improve the localization. We tested this with cWB and observed no change in the 2015 data set. This is because the two-detector regulator values force the algorithm to reconstruct signals with a single polarization, and knowledge that the signal is circularly polarized adds nothing. However, in the three-detector network, we see that the median searched area improves by nearly a factor of 3, from 112.5 deg^2 to 38.0 deg^2 . With the polarization constraint, this is comparable to the localization observed with lighter systems using matched filtering techniques [Singer et al. (2014)]. However, Singer et al. (2014) focus on different sources than our BBH injection set and a direct comparison between our results requires careful consideration.

Customizing gravitational-wave searches to specific source models may improve our ability to localize them in the sky in a significant way.

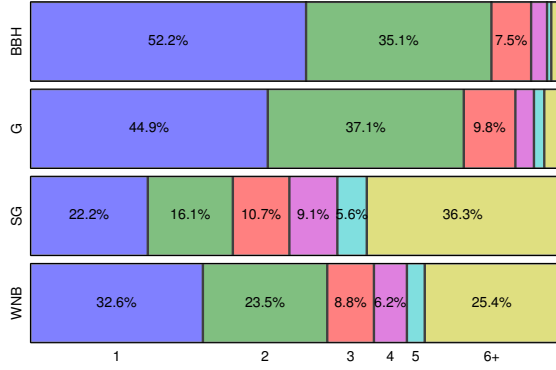
5. SYSTEMATICS

We have investigated several sources of potential systematics in cWB's and LIB's reconstructed sky positions. These can be roughly classified as "calibration" and "accuracy" biases.

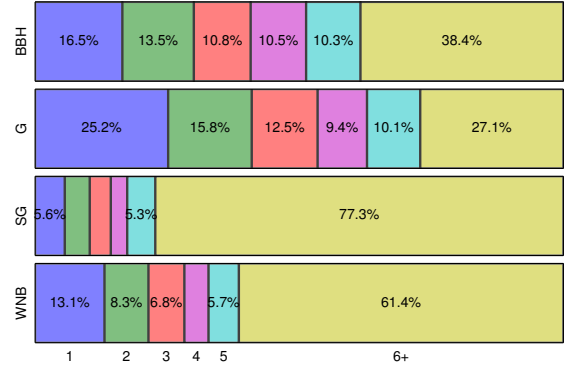
5.1. Posterior calibration

We first study systematics associated with the probability assigned by the localization algorithms on a pixel-by-pixel basis. This can be considered a "calibration" problem with the posterior distributions over the sky. On average, we expect the confidence region containing N% cumulative probability to contain N% of the detected injections.

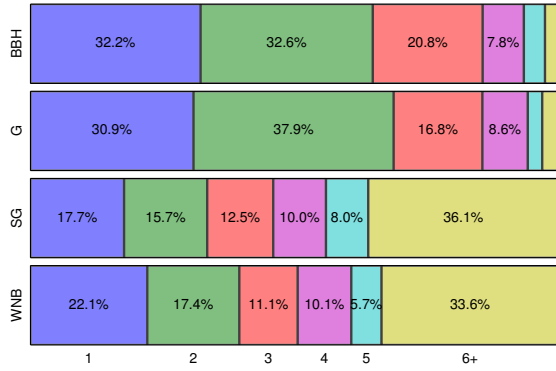
For cWB we find the calibration of the posterior distributions to depend strongly on the choice of regulators, in addition to its dependence on the intrinsic parameters of the simulated events. The dependence on the regulators seems to dominate these systematics. We have seen variation in frequentist confidence levels as large as 50% in both directions, i.e., undercovering and overcovering. For the specific choice of regulators (Section 7.2), cWB generally underestimates the actual confidence at low confidence levels and overestimates the actual confidence at very high confidence levels. cWB's 50% confidence regions contain between 65%-85% of the detected signals in 2015 and between 65%-75% of detected signals



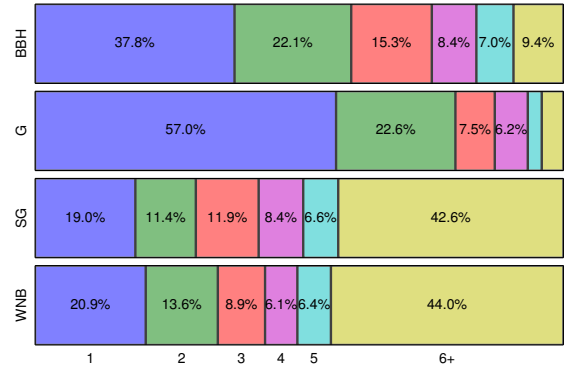
(a) cWB HL 2015



(b) cWB HLV 2016



(c) LIB HL 2015



(d) LIB HLV 2016

FIG. 6.— Fractions of events binned by the number of disjoint regions in the searched area. (a,c) 2015 HL and (b,c) 2016 HLV. (a,b) cWB. (c,d) LIB. SG signals typically have more modes because they support fringe peaks.

TABLE 2
TABULAR SUMMARY OF cWB LOCALIZATION. STATISTICAL ERROR IS ON THE ORDER A FEW PERCENT.

year network morphology	2015 HL				2016 HLV			
	BBH	SG	G	WNB	BBH	SG	G	WNB
fraction (in %) with searched area less than								
5 deg ²	3.1	3.4	3.1	6.2	6.7	9.3	12.0	17.2
20 deg ²	11.5	12.7	10.9	17.8	18.9	22.2	28.8	32.5
100 deg ²	35.3	37.2	37.1	51.8	47.3	52.3	54.9	61.3
200 deg ²	51.6	52.2	49.2	69.7	62.3	66.9	69.1	75.8
500 deg ²	75.9	69.2	73.8	86.5	82.2	85.8	84.9	91.2
1000 deg ²	89.2	82.2	87.1	95.6	93.1	94.8	95.0	98.0
fraction (in %) with $\delta\theta$ less than								
1°	1.3	1.4	0.8	2.7	3.6	2.8	9.8	10.0
5°	12.9	8.5	11.7	13.0	22.6	13.0	29.3	19.0
15°	37.2	27.1	33.2	34.1	37.6	26.4	45.8	32.6
45°	73.1	61.4	66.0	70.9	61.3	57.3	67.9	59.2
60°	79.5	68.4	71.1	74.9	66.7	62.2	71.7	64.7
90°	83.1	74.0	75.8	77.9	71.4	67.1	74.3	70.0
median searched area	184.6 deg ²	181.6 deg ²	209.9 deg ²	93.0 deg ²	112.5 deg ²	91.7 deg ²	71.3 deg ²	61.3 deg ²
median $\delta\theta$	23.1°	31.6°	25.7°	23.9°	27.5°	36.7°	18.6°	33.9°

TABLE 3
 TABULAR SUMMARY OF LIB LOCALIZATION. STATISTICAL ERROR IS ON THE ORDER OF A FEW PERCENT.

year network morphology	2015 HL				2016 HLV				
	BBH	SG	G	WNB	BBH	SG	G	WNB	
fraction (in %) with searched area less than	5 deg ²	1.8	4.0	2.3	4.7	8.6	25.5	18.5	10.4
	20 deg ²	9.4	14.3	7.0	14.2	23.1	47.4	43.0	23.9
	100 deg ²	31.8	39.0	34.8	35.2	53.8	75.8	73.6	46.8
	200 deg ²	46.8	52.9	49.2	51.2	65.7	84.6	84.4	59.2
	500 deg ²	70.2	71.7	72.7	65.1	82.9	92.6	93.3	69.8
	1000 deg ²	88.2	82.6	89.1	74.9	93.0	94.9	97.4	76.0
fraction (in %) with $\delta\theta$ less than	1°	1.0	2.1	1.2	2.1	6.2	11.4	12.0	5.5
	5°	8.6	8.8	11.7	9.5	34.5	31.9	51.4	17.2
	15°	32.2	25.8	30.1	28.6	54.6	53.8	66.8	31.3
	45°	66.8	63.7	63.7	61.9	77.1	78.3	83.7	63.6
	60°	72.8	71.0	68.8	67.2	81.3	81.8	85.8	70.1
	90°	77.4	75.9	74.2	70.4	83.7	84.6	86.5	76.2
median searched area	238.5 deg ²	171.0 deg ²	208.4 deg ²	180.9 deg ²	82.5 deg ²	22.2 deg ²	31.3 deg ²	121.3 deg ²	
median $\delta\theta$	26.6°	29.4°	27.1°	30.4°	11.1°	13.3°	4.9°	27.5°	

in 2016, depending on morphology. Because the choice of regulators will depend on the character of real data, systematics and the regulators' impact on localization and detection efficacy need to be re-evaluated when advanced LIGO and Virgo will come online. This may include recalibration to account for observed systematics.

LIB also shows calibration issues. Its 50% confidence regions contain between 45%-55% of the detected signals in 2015 and between 35%-45% of detected signals in 2016, depending on morphology. LIB's systematic overestimation of the actual confidence observed in the 2016 data is due to differences in the population of detected events and the population expected by LIB's priors. We have verified that when detected events sample LIB's uniform-in-volume prior, LIB's posteriors are properly calibrated. Selection effects in events detected by cWB may result in such deviations from the assumed prior.

Such calibration issues are not particular to burst searches, and are observed with localization pipelines targeting binary neutron star coalescences [Sidery et al. (2014)]. Although these systematics warrant further investigation, they do not imply that these algorithms cannot be used to direct electromagnetic follow-up of gravitational wave events. Any observing plan consists of a set of fields sorted by an ordinal function of their probability to contain signal. The observing strategy will not depend on the actual function, as long as it preserves ordering.

5.2. Bias in reconstructed positions

We also compared the distribution of injected positions for detected events against their estimated positions. We expect these distributions to match over an ensemble average, implying the algorithms typically localize signals to the same regions of the sky from which they are detected. The injected positions of detected events always follow the antenna patterns of our network of detectors. We therefore expect the reconstructed positions to similarly follow the antenna patterns.

Both algorithms behave essentially as expected in the two-detector case (2015). However, we observe a bias in cWB's estimated positions in the three-detector network (2016). As with the calibration of the posteriors (Section 5.1), the size and direction of this bias depends strongly on the choice of regulators. The estimated sky positions may be clumped into regions with different shapes than the injected distributions and may not coincide with the maxima of the antenna patterns. For the regulators used in this study, this offset corresponds to between 20° and 40° . This bias is also imprinted on the entire posterior and not just the maxima. We also note that, when applying a circular polarization constraint in cWB, the median searched area improves and the bias is removed. We do not observe any such bias with LIB, which may partially account for the increased disagreement with cWB in the 2016 data.

6. CONCLUSIONS

We present a study of gravitational-wave source localization capabilities for un-modeled signals during the early advanced LIGO and Virgo detector era. In particular, we focus on the transition from two operational detectors in 2015 to three operational detectors in 2016,

and quantify the improvement in localization associated therewith. In performing this study we used two different localization algorithms: Coherent WaveBurst (cWB), a low-latency maximum likelihood algorithm, and LALInferenceBurst (LIB), a Markov chain Monte Carlo (MCMC) parameter estimation algorithm. We used four signal morphologies to explore a wide range of possible signals detectable by generic burst searches.

We find that, while there is some variation with waveform morphologies, 50% of injected signals would be imaged after observing 100-200 deg^2 with two detectors in 2015. We find that cWB can reduce this to within 60-110 deg^2 in 2016 with low latency, and LIB may reduce the median searched area to as little as 22 deg^2 when the signal matches the template. Tables 2 and 3 summarize our findings. While the searched areas may be small, we should remember that the posterior may be spread across large portions of the sky, including antipodal points.

Importantly, we also introduce an effective prior on the source position due to anisotropic antenna patterns and knowledge of signal amplitude distributions. With this prior, we find cWB performs comparably to the full MCMC LIB algorithm in the two-detector configuration (2015) with significantly lower latency. This is true even for signal morphologies that correspond to LIB's templates. However, LIB significantly improves upon rapid localizations provided by cWB with three detectors (2016) for most of the considered morphologies.

Furthermore, we find that cWB systematically localizes WNB signals more accurately than LIB. This is because cWB makes no assumption on the signal morphology while LIB assumes a single SG template. cWB localizes WNB signals better than SG or G signals because of differences in the signal morphologies. We expect high-frequency or large bandwidth signals to be the better localized than low-frequency or narrow bandwidth signals.

We also studied the posteriors produced by cWB and LIB on an event-by-event basis. We found that the two algorithms agree on the maximum a posteriori points to a remarkable degree in 2015, typically to within 8° . We find that the selected pixels agree to over 50% in the two-detector network, but agree significantly less in the three-detector network. Several considerations lead us to the heuristic conclusion that LIB posteriors are typically sharply peaked with long tails and large spatial support. cWB posteriors are typically less peaked, more uniform with smaller spatial support.

Finally, we investigate and quantify some systematics with both methods. Both cWB and LIB show calibration issues with their posteriors, in that the Bayesian confidence regions do not correspond to their frequentist counterparts. cWB's regulators introduce biases in the reconstructed positions in the 2016 data set, and in a small fraction of events modulate the posterior so strongly that the source's location is outside of the posterior's support.

We expect templated searches targeting known signal morphologies to localize signals more accurately than generic un-modeled searches. When compared to an analogous study focusing on Binary Neutron Star (BNS) coalescences [Singer et al. (2014)], we see that the localization of BNS signals is indeed more accurate than generic bursts. However, the generic burst searches pro-

duce median searched areas that are only a factor of 2-3 larger than BNS median searched areas. In fact, the median searched areas may be comparable if the actual burst waveform is known reasonably well in the three-detector network, such as LIB recovering SG injections. For circularly polarized signals, cWB can achieve comparable results if it assumes the signal is circularly polarized. While this study and Singer et al. (2014) both use populations distributed uniformly in volume, we investigate very different signal morphologies. Furthermore, Singer et al. (2014) estimates the detectors duty cycles in 2016 and occasionally detect events with only two detectors instead of all three. This could cause our estimates to seem more similar than they really are. However, we also use a lower false-alarm rate threshold than Singer et al. (2014), which will increase our error estimates systematically because we will include quieter events. Any direct comparison between these studies should include careful consideration of such differences.

Importantly, we find that telescope networks attempting to follow up BNS events from advanced gravitational wave detectors by searching large error areas can search

the comparably sized areas for burst events. Given the nature of such generic events, electromagnetic observations will be instrumental in placing gravitational wave observations in an astrophysical context.

ACKNOWLEDGEMENTS

The authors would like to thank J. Veitch and A. Vecchio for comments and suggestions about LIB, W. Farr for his script to convert MCMC posterior samples into a pixelated posterior as well as R. Vaulin and R. Lynch for many useful discussions throughout the course of this research. The authors also acknowledge L. Price for helpful comments when preparing this manuscript and L. Singer for creating the 2015 Gaussian noise data. LIGO was constructed by the California Institute of Technology and Massachusetts Institute of Technology with funding from the NSF and operates under cooperative agreement PHY-0757058. This work was also supported from NSF awards PHY-1205512 and PHY-0855313 to the University of Florida.

REFERENCES

- Aasi, J. 2014a, *The Astrophysical Journal Supplement Series*, 211, 7
- Aasi, J., Abadie, J., Abbott, B. P., et al. 2013, *Phys. Rev. D*, 88, 062001
- Aasi, J. e. a. 2014b, *Phys. Rev. Lett.*, 112, 131101
- Abadie, J. 2012a, *Phys. Rev. D*, 85, 082002
- Abadie, J. e. a. 2012b, *Phys. Rev. D*, 85, 122007
- . 2012c, *A&A*, 541, A155
- Accadia, T., Acernese, F., Alshourbagy, M., et al. 2012, *Journal of Instrumentation*, 7, 3012
- Ajith, P., Iyer, B. R., Robinson, C. A. K., & Sathyaprakash, B. S. 2005, *Classical and Quantum Gravity*, 22, S1179
- Ajith, P., Hannam, M., Husa, S., et al. 2011, *Phys. Rev. Lett.*, 106, 241101
- Barnes, J., & Kasen, D. 2013, *The Astrophysical Journal*, 775, 18
- Belczynski, K., Buonanno, A., Cantiello, M., et al. 2014, *The Astrophysical Journal*, 789, 120
- Burrows, A., Dessart, L., Livne, E., Ott, C. D., & Murphy, J. 2007, *The Astrophysical Journal*, 664, 416
- Burrows, A., Livne, E., Dessart, L., Ott, C. D., & Murphy, J. 2006, *The Astrophysical Journal*, 640, 878
- Cannon, K., Emberson, J. D., Hanna, C., Keppel, D., & Pfeiffer, H. P. 2013, *Phys. Rev. D*, 87, 044008
- Damour, T., & Nagar, A. 2008, *Phys. Rev. D*, 77, 024043
- Dimmelmeier, H., Ott, C. D., Marek, A., & Janka, H.-T. 2008, *Phys. Rev. D*, 78, 064056
- Dominik, M., Belczynski, K., Fryer, C., et al. 2012, *ApJ*, 759, 52
- Evans, P. A. e. a. 2012, *The Astrophysical Journal Supplement Series*, 203, 28
- Fairhurst, S. 2009, *New Journal of Physics*, 11, 123006
- . 2011, *Classical and Quantum Gravity*, 28, 105021
- Feng, L., Vaulin, R., & Hewitt, J. 2014, arXiv:1405.6219
- Hannam, M., Husa, S., Ohme, F., Müller, D., & Brüggmann, B. 2010, *Phys. Rev. D*, 82, 124008
- Harry, G. M., & the LIGO Scientific Collaboration. 2010, *Classical and Quantum Gravity*, 27, 084006
- J. Aasi, e. a. 2013, arXiv:1304.0670, LIGO-P1200087, VIR-0288A-12
- J Aasi, e. a. 2014, *Classical and Quantum Gravity*, 31, 115004
- J. Smith, e. a. 2014
- Kelley, L. Z., Ramirez-Ruiz, E., Zemp, M., Diemand, J., & Mandel, I. 2010, *ApJ*, 725, L91
- Klimenko, S. 2014, in preparation
- Klimenko, S., Mohanty, S., Rakhmanov, M., & Mitselmakher, G. 2005, *Phys. Rev. D*, 72, 122002
- Klimenko, S., Yakushin, I., Mercer, A., & Mitselmakher, G. 2008, *Classical and Quantum Gravity*, 25, 114029
- Klimenko, S., Vedovato, G., Drago, M., et al. 2011, *Phys. Rev. D*, 83, 102001
- LIGO Scientific Collaboration, Virgo Collaboration, Abadie, J., et al. 2012, *A&A*, 539, A124
- LIGO Scientific Collaboration, Virgo Collaboration. 2014, www.lsc-group.phys.uwm.edu/daswg/projects/lal/nightly/docs/html/group_pkg_lal_inference.html
- Logue, J., Ott, C. D., Heng, I. S., Kalmus, P., & Scargill, J. H. C. 2012, *Phys. Rev. D*, 86, 044023
- Markowitz, J., Zanolin, M., Cadonati, L., & Katsavounidis, E. 2008, *Phys. Rev. D*, 78, 122003
- Metzger, B. D., & Berger, E. 2012, *ApJ*, 746, 48
- Ott, C. D. 2009, *Classical and Quantum Gravity*, 26, 063001
- Ott, C. D., Burrows, A., Dessart, L., & Livne, E. 2006, *Phys. Rev. Lett.*, 96, 201102
- Scholberg, K. 2012, *Annual Review of Nuclear and Particle Science*, 62, 23
- Sidery, T., Aylott, B., Christensen, N., et al. 2014, *Phys. Rev. D*, 89, 084060
- Singer, L. P., Price, L. R., Farr, B., et al. 2014, ArXiv e-prints, 1404.5623
- Skilling, J. 2004, in *American Institute of Physics Conference Series*, Vol. 735, American Institute of Physics Conference Series, ed. R. Fischer, R. Preuss, & U. V. Toussaint, 395–405
- Sturani, R., Fischetti, S., Cadonati, L., et al. 2010, *Journal of Physics: Conference Series*, 243, 012007
- Sutton, P. J., Jones, G., Chatterji, S., et al. 2010, *New Journal of Physics*, 12, 053034
- Vachaspati, T. 2008, *Phys. Rev. Lett.*, 101, 141301
- Veitch, J., Raymond, V., Farr, B., et al. 2014, In preparation
- Veitch, J., & Vecchio, A. 2010, *Phys. Rev. D*, 81, 062003
- Vitale, S. 2014, in preparation

7. APPENDIX

7.1. Injection parameter ranges

Table 4 lists the injection parameter ranges and distributions used. Definition of the waveform morphologies are provided in Section 2.

TABLE 4
INJECTION POPULATION PARAMETERS

		minimum	maximum	distribution
SG	f_o	40 Hz	1500 Hz	$dn \propto constant$
	$Q = \sqrt{2\pi}\tau f_o$	3	30	
	$\cos(\alpha)$	0	1	
	ϕ_o	0	2π	
h_{rss}	2015	$3.0000 \cdot 10^{-23} Hz^{-1/2}$	$1 \cdot 10^{-15} Hz^{-1/2}$	$dn \propto D_L^2 dD_L \propto h_{rss}^{-4} dh_{rss}$
	2016	$2.0625 \cdot 10^{-23}, Hz^{-1/2}$	$1 \cdot 10^{-15} Hz^{-1/2}$	
G	τ	1 ms	10 ms	$dn \propto constant$
	$\cos(\alpha)$	0	1	
h_{rss}	2015	$4.0000 \cdot 10^{-23} Hz^{-1/2}$	$1 \cdot 10^{-15} Hz^{-1/2}$	$dn \propto h_{rss}^{-4} dh_{rss}$
	2016	$2.7500 \cdot 10^{-23} Hz^{-1/2}$	$1 \cdot 10^{-15} Hz^{-1/2}$	
WNB	τ	5 ms	100 ms	$dn \propto constant$
	$f_o \sim (f_{max} + f_{min})/2$	40 Hz	1500 Hz	
	$\sigma_f \sim (f_{max} - f_{min})/2$	10 Hz	500 Hz	
h_{rss}	2015	$4.0000 \cdot 10^{-23} Hz^{-1/2}$	$1 \cdot 10^{-15} Hz^{-1/2}$	$dn \propto h_{rss}^{-4} dh_{rss}$
	2016	$2.7500 \cdot 10^{-23} Hz^{-1/2}$	$1 \cdot 10^{-15} Hz^{-1/2}$	
BBH	M_1	15 M_\odot	25 M_\odot	$dn \propto constant$
	M_2	15 M_\odot	25 M_\odot	
	S_1	0.0	0.9	
	S_2	0.0	0.9	
z	2015	10^{-4}	0.2218	$dn \propto \frac{dV_{comov}}{dz} dz$
	2016	10^{-4}	0.33	

7.2. Algorithmic parameters

We used version 3481M of the cWB repository, searching for signals with frequencies between 32-2048 Hz. Our detection thresholds were set to $\rho = 8.0$, netcc=0.7. While false-alarm rates will depend on the noise in our detectors, these detections correspond to a false-alarm-rate of 1 yr^{-1} in historical non-Gaussian noise. Table 5 lists the regulator values used in this study, which we varied depending on the detector network. We note that the regulators in 2015 force cWB to reconstruct a single polarization, while the regulators in 2016 are almost, but not quite, turned off. The consequences of $\delta \neq 0$ in 2016 are discussed in Section 5

TABLE 5
COHERENTWAVEBURST SEARCH PARAMETERS.

year/network	SVN revision No.	cWB version	f_{low}	f_{high}	ρ	netCC	δ	γ
2015/HL	3481M	2G	32 Hz	2048 Hz	8.00	0.70	-10^{40}	0.5
2016/HLV							0.05	0.5

We ran LIB with three parallel chains with 500 live points each, and estimated noise power spectral densities from the data separately for each event using 96 seconds near the trigger time. Table 6 list the prior ranges used for LIB's SG template.

7.3. Derivation of effective priors

We can write down an astrophysically motivated prior, such as a uniform in co-moving volume distribution. However, for burst signals, we do not immediately have a good estimate for the distance (D) or the energy scale (E). We can relate this to the observed data (h) through

$$\frac{E}{D^2} \propto \int df f^2 (|h_+|^2 + |h_\times|^2) \quad (9)$$

To obtain a prior on h , we should marginalize over all possible D and E .

TABLE 6
LALINFERENCEBURST PRIOR RANGES

	$\log(h_{rss})$	f_o	Q	α	ϕ
minimum	-53.0	1 Hz	2	0	0
maximum	-46.5	1300 Hz	35	2π	2π
distribution	$p(h_{rss}) \propto h_{rss}^{-4}$	$p(f_o) \propto \text{constant}$	$p(Q) \propto \text{constant}$	$p(\alpha) \propto \text{constant}$	$p(\phi) \propto \text{constant}$

$$p(h, E, D)dh dE dD = p(h|E, D)dh \cdot p(E)dE \cdot p(D)dD \quad (10)$$

$$\propto \delta\left(h - \lambda\sqrt{\frac{E}{D^2}}\right) dh \cdot p(E)dE \cdot D^2dD \quad (11)$$

$$(12)$$

where $h^2 = \int df f^2 (|h_+|^2 + |h_\times|^2)$ and λ is a proportionality constant. Marginalization yields

$$p(h) \propto \int dE p(E) \int dD D^2 \delta\left(h - \lambda\sqrt{\frac{E}{D^2}}\right) \quad (13)$$

$$\propto \int dE p(E) \int dD D^2 \delta\left(D - \lambda\sqrt{\frac{E}{h^2}}\right) \frac{\lambda\sqrt{E}}{h^2} \quad (14)$$

$$\propto h^{-4} \lambda^3 \int dE p(E) E^{3/2} \quad (15)$$

$$\propto h^{-4} \quad (16)$$

Because we do not know the actual waveform a priori, we must marginalize over the waveform to compute the posterior. With a small number of detectors, the likelihood is not strongly peaked around the maximum likelihood estimate and we can approximate

$$\int dh p(h) \sim h_{ML}^{-3} \quad (17)$$

where h_{ML} is the maximum likelihood reconstructed signal. This can be approximated by $h_{ML} \sim (F_+^2 + F_\times^2)^{-1/2}$, where $F_{+, \times}$ are the antenna patterns for the entire network in the dominant polarization frame [Klimentko et al. (2011); Sutton et al. (2010)]. We then expect the effective prior on (θ, ϕ) to be something like

$$p_{\text{eff}}(\theta, \phi) = (F_+^2 + F_\times^2)^{3/2} \quad (18)$$

We observe that this prior improves source localization, although there is only a weak dependence on the actual exponent used. For most signals, any positive power of the antenna patterns tends to order the pixels in the correct way to reduce the searched area. However, the posterior's calibration depends strongly on this exponent. cWB's regulators skew it's calibration and the two affects are difficult to separate.

7.4. Sample posteriors

Figure 7 demonstrates posterior distributions produced by both cWB and LIB for WNB injections. In the two-detector examples, we can clearly see fringe peaks characteristic of high-frequency, low-bandwidth signals. The two-detector injection has a central frequency of ~ 560 Hz, which corresponds to an angular scale of $\sim 10^\circ$. The three-detector injection has a central frequency of ~ 350 Hz, which corresponds to $\sim 16^\circ$ between the two LIGO detectors and $\sim 6^\circ$ between the LIGO's and Virgo. We also see that LIB and cWB agree, but LIB's posterior is "fuzzy," which we expect due to template mismatch. The three-detector network shows similar fringe structures, although now we can see the main triangulation ring from the two LIGO detectors modulated by information from Virgo. In the LIB posterior, we can even see the regular lattice imprinted on neighbouring triangulation rings. We note that the three-detector posteriors are less similar than the two-detector posteriors, which we discuss in detail in Sections 4.5 and 5.

Figure 8 is analogous to Figure 7, except it shows data from BBH injections. For BBH injections, which have wide bandwidths relative to their central frequencies, we do not expect fringe peaks. The modulation in the three-detector network along the single triangulation ring is caused by Virgo. The cWB posteriors clearly demonstrate the increase in the number of disjoint regions when progressing from the two-detector network to the three-detector network.

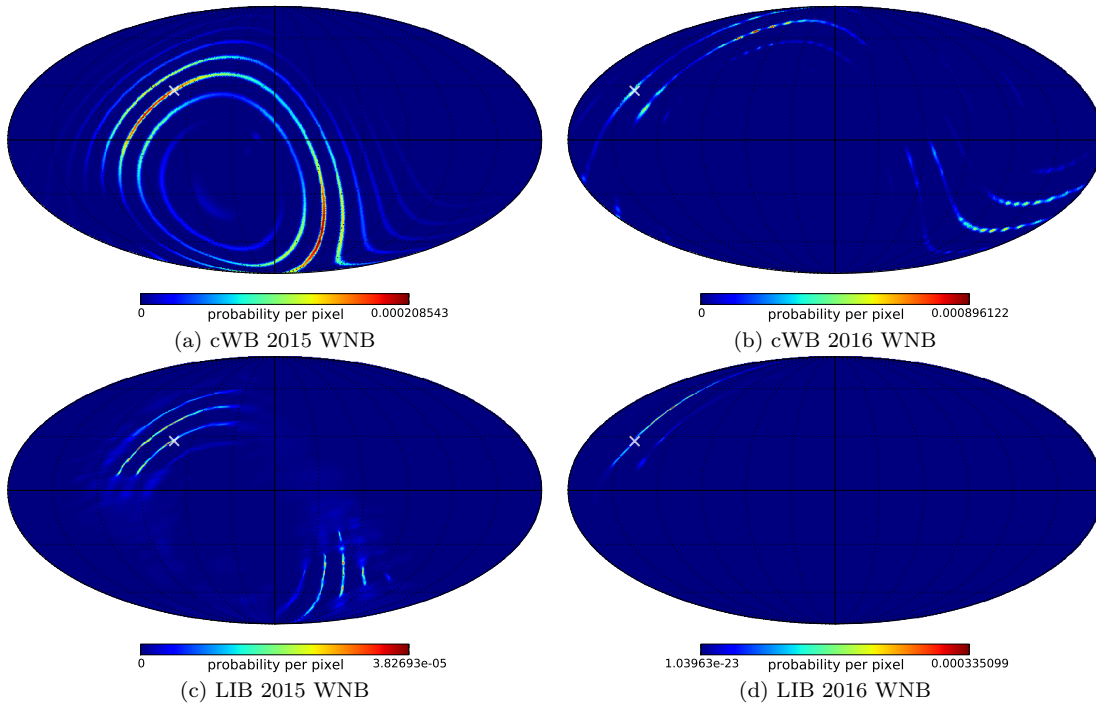


FIG. 7.— Sample WNB posteriors. (a,c) 2015. (b,d) 2016. (a,b) cWB. (c,d) LIB. An “x” marks the injected location. These are mollweide “geo” projections. The 2015 injection had SNRs of 8.81, 11.72 and 14.66 for LHO, LLO, and the entire network, respectively. The 2016 injection had SNRs of 13.02, 10.66, 1.65 and 16.91 for LHO, LLO, Virgo and the entire network, respectively.

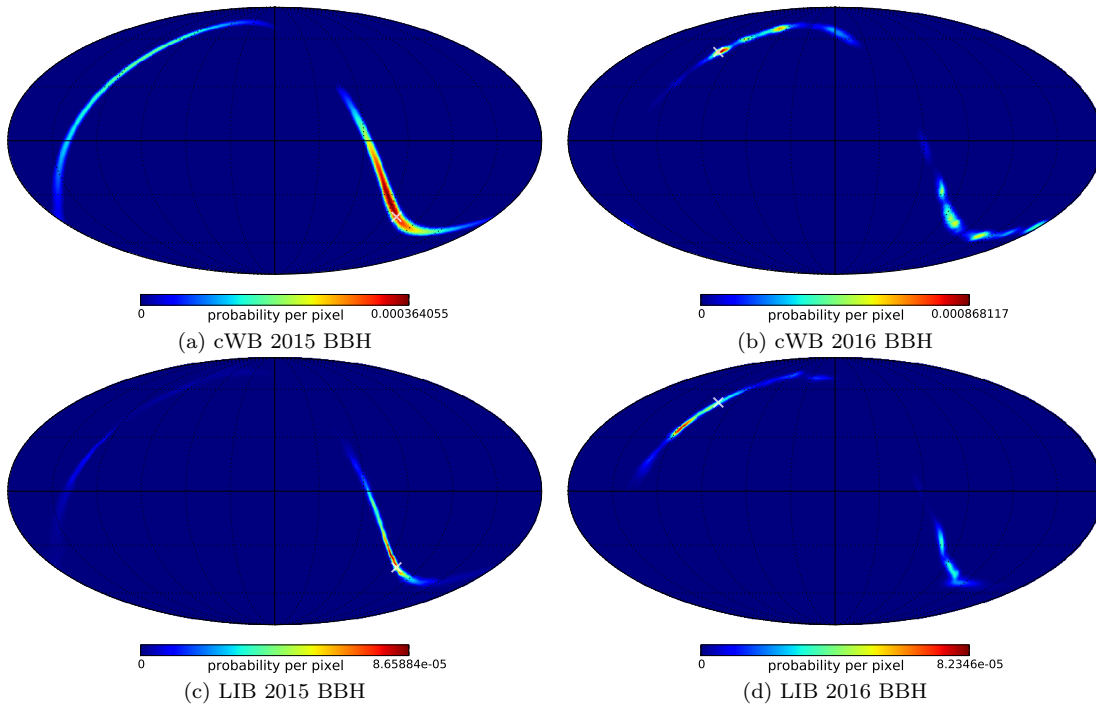


FIG. 8.— Sample BBH posteriors. (a,c) 2015. (b,d) 2016. (a,b) cWB. (c,d) LIB. An “x” marks the injected location. These are mollweide “geo” projections. The 2015 injection had SNRs of 11.37, 12.72, and 17.06 for LHO, LLO, and the entire network, respectively. The 2016 injection had SNRs of 14.06, 13.40, 1.85 and 19.51 for LHO, LLO, Virgo and the entire network, respectively.